UC Irvine
UC Irvine Previously Published Works

Title

Loss of SLC25A46 causes neurodegeneration by affecting mitochondrial dynamics and energy production in mice.

Permalink

https://escholarship.org/uc/item/1d29m7v9

Journal

Human molecular genetics, 26(19)

ISSN

0964-6906

Authors

Li, Zhuo
Peng, Yanyan
Hufnagel, Robert B
et al.

Publication Date

2017-10-01

DOI

10.1093/hmg/ddx262

Copyright Information

Peer reviewed

ORIGINAL ARTICLE

Loss of SLC25A46 causes neurodegeneration by affecting mitochondrial dynamics and energy production in mice

Zhuo Li[1,2], Yanyan Peng[1], Robert B. Hufnagel[1], Yueh-Chiang Hu[3], Chuntao Zhao[4], Luis F. Queme[5], Zaza Khuchua[6], Ashley M. Driver[1], Fei Dong[7], Q. Richard Lu[4], Diana M. Lindquist[8], Michael P. Jankowski[5], Rolf W. Stottmann[1], Winston W.Y. Kao[7] and Taosheng Huang[1,*]

[1]Division of Human Genetics, Cincinnati Children's Hospital Medical Center, Cincinnati, OH 45229, USA, [2]State Key Laboratory of Medical Genetics, School of Life Sciences, Central South University, Changsha, Hunan 410078, China, [3]Division of Developmental Biology, [4]Division of Experimental Hematology and Cancer Biology, Brain Tumor Center, Cancer and Blood Diseases Institute, [5]Division of Anesthesia, [6]Division of Molecular Cardiovascular Biology, Cincinnati Children's Hospital Medical Center, Cincinnati, OH 45229, USA, [7]Department of Ophthalmology, University of Cincinnati, Cincinnati, OH 45267, USA and [8]Department of Radiology, Cincinnati Children's Hospital Medical Center, Cincinnati, OH 45229, USA

*To whom correspondence should be addressed at: Division of Human Genetics, Cincinnati Children's Hospital Medical Center, 3333 Burnet Avenue, Cincinnati, OH 45229, USA. Tel: 513 8039260; Fax: 513 8039271; Email: taosheng.huang@cchmc.org

Abstract

Recently, we identified biallelic mutations of *SLC25A46* in patients with multiple neuropathies. Functional studies revealed that SLC25A46 may play an important role in mitochondrial dynamics by mediating mitochondrial fission. However, the cellular basis and pathogenic mechanism of the SLC25A46-related neuropathies are not fully understood. Thus, we generated a *Slc25a46* knock-out mouse model. Mice lacking SLC25A46 displayed severe ataxia, mainly caused by degeneration of Purkinje cells. Increased numbers of small, unmyelinated and degenerated optic nerves as well as loss of retinal ganglion cells indicated optic atrophy. Compound muscle action potentials in peripheral nerves showed peripheral neuropathy associated with degeneration and demyelination in axons. Mutant cerebellar neurons have large mitochondria, which exhibit abnormal distribution and transport. Biochemically mutant mice showed impaired electron transport chain activity and accumulated autophagy markers. Our results suggest that loss of SLC25A46 causes degeneration in neurons by affecting mitochondrial dynamics and energy production.

Introduction

Mitochondria are highly dynamic organelles that are essential for aerobic metabolism and energy production. Recently, we identified SLC25A46, a mitochondrial outer member protein, as a new mitochondrial dynamics-related gene (1). Recessive mutations in *SLC25A46* in patients displayed cerebellar atrophy, peripheral neuropathy, and optic atrophy (1). This disorder spectrum has been defined as neuropathy, hereditary motor and sensory, Type VIB (HMSN6B), in Online Mendelian Inheritance in Man (OMIM)

(http://www.omim.org/entry/616505; date last accessed July 13, 2017). Subsequent reports showed *SLC25A46* mutations cause multiple neuropathies, optic atrophy, Leigh syndrome, progressive myoclonic ataxia and lethal congenital pontocerebellar hypoplasia (2–5). Our previous functional study demonstrated the role for SLC25A46 in mitochondrial fission, possibly mediated by protein networks different from the MFN2-OPA1 fusion complex (1). Recent studies based on non-neuron cell models showed that SLC25A46 may have other functions in mitochondrial dynamics by regulating contacts between the endoplasmic reticulum (ER) and mitochondria or serves as a regulator for MFN1/2 oligomerization (3,6).

Mitochondrial dynamics (fusion and fission) affect not only their morphology, but also mitochondrial function and distribution within the cell, which are related to cell bioenergetics and cell damage. Neurons are particularly sensitive to control of mitochondrial distribution (7), since neurons often have long processes and require proper transportation of mitochondria across long distances to meet the energy requirements of electrical excitability and synaptic transmission. Increasing evidence suggests that abnormal mitochondrial dynamics contribute to neurodegenerative and metabolic disorders (8–11). For example, mutations in *MFN1/2* and *OPA1* in patients cause Charcot-Marie-Tooth neuropathy type 2A (CMT2A) (12–14) and autosomal dominant optic atrophy (ADOA), respectively (8,15,16). A dominant-negative allele of *DRP1* was reported to be associated with abnormal brain development, optic atrophy, and various other abnormalities (17). However, different fusion/fission-related proteins may affect different neurons in a tissue-specific manner. For example, mutations in *MFN1/2* mainly affect the motor and sensory neurons (12–14), whereas mutations in *OPA1* usually affect optic nerve (8,15,16). Loss of OPA1 function leads to mitochondrial fragmentation and increased apoptosis (18,19), but apoptosis is generally not affected in MFN1/2 -deficient cells (20,21). Cerebellar cortex abnormalities and Purkinje cells (PCs) degeneration were specifically associated with *MFN* or *DRP1* mutations (22–25). There is also evidence of a link between *DRP1* and autophagy (26,27). Nevertheless, the deficiency of mitochondrial dynamics is common for these conditions. At present, management of these mitochondrial disorders and neurodegenerative disorders remains challenging (28) and highlights the importance of identifying the cellular pathogenesis in the animal model for developing therapeutic targets.

Our recent studies demonstrated a clear connection in zebrafish model between multiple neuropathies in patients with *SLC25A46* mutations and the balance of mitochondrial dynamics (1). Nevertheless, the cellular and molecular basis and pathogenic mechanism of this connection are not fully understood. For example, which specific neuronal populations are particularly sensitive to loss of SLC25A46? How does SLC25A46 deficiency affect mitochondrial functions in specific neurons? How do the affected mitochondria, in turn, induce neuronal fate? To address these questions, we generated the *Slc25a46* knock-out mouse model by CRISPR/Cas9 technology. Our findings suggest that SLC25A46 play an important role in mitochondrial morphogenesis, function, and transport as well as autophagy in mammalian neurons. *Slc25a46* mutations result in notable degeneration in specific neurons, leading to multiple neuropathies.

Results

Slc25a46 mutation causes severe ataxia in the mouse model

We and others previously determined that mutations in *SLC25A46* are causative of a disorder spectrum with cerebellar atrophy, peripheral neuropathy, and optic atrophy (1–5), but the underlying pathogenesis of these mutations in mammals remains unknown. Here, we generated a transgenic knock-out mouse model by inducing a 46-bp deletion in exon 8 of *Slc25a46* with CRISPR/Cas9 technology (homozygous knock-out mice described as *Slc25a46*$^{-/-}$, heterozygous as *Slc25a46*$^{+/-}$ and wild type as WT). The deletion causes a frameshift and a subsequent stop codon 15 amino acids downstream (Fig. 1A; Supplementary Material, Fig. S1A). To confirm loss of SLC25A46 at the protein level, we performed Western blot analysis. As shown in (Fig. 1B), *Slc25a46*$^{-/-}$ showed absence of the SLC25A46 protein and high levels of SLC25A46 were noticed in wild-type. Specificity of anti-human SLC25A46 was tested with cell lines overexpressing the SLC25A46 protein (Supplementary Material, Fig. S1B).

Viable pups were born at the expected Mendelian inheritance ratios. *Slc25a46*$^{-/-}$ mice appeared normal and there were no obvious phenotypes in the embryos nor in the early postnatal periods (Supplementary Material, Fig. S1C and D). However, beginning at postnatal day 14 (P14), both males and females of *Slc25a46*$^{-/-}$ mice developed a progressively unstable gait, smaller body size and short lifespan, compared to their wild-type littermates (Fig. 1C–E). Mutant mice frequently fell and tilted to one side when walking (Supplementary Material, Movie.1). Most adult *Slc25a46*$^{-/-}$ mice displayed weak motor activity and were unable to maintain an upright position. To prevent malnutrition from an inability to reach food due to poor motor coordination, we manually placed all animals on diets with DietGel inside the cage. Nevertheless, more than 70% of *Slc25a46*$^{-/-}$ mice died prematurely between 2 and 8 weeks of age ($P < 0.001$) (Fig. 1E), partially due to seizure-like activities which could be induced by environmental interference (Supplementary Material, Movie. 2). Few *Slc25a46*$^{-/-}$ mice survived beyond 6 months of age.

To assess motor coordination in more detail, *Slc25a46*$^{-/-}$ and WT littermates were subjected to rotarod testing at 4 weeks after birth. *Slc25a46*$^{-/-}$ mice exhibited a significant reduction in time spent on the rotarod ($P < 0.001$), indicating impaired balance and motor coordination (Fig. 1F). Locomotor testing within 60 min confirmed the significantly lower motor activity for *Slc25a46*$^{-/-}$ mice ($P < 0.001$) (Fig. 1G).

Purkinje cell loss and dendritic abnormalities are associated with ataxia in *Slc25a46*$^{-/-}$ mice

To explore the underlying pathological change leading to ataxia and abnormal gait, we searched for anatomical and histological abnormalities from *Slc25a46*$^{-/-}$ cerebellum, which mainly functions in control of motor coordination and balance. At 2 and 9 weeks of age, the neural architecture of the mutant brain was grossly normal. Except for the smaller size of the brain in adult mutant mice, there were no visible defects in the structure of the vermis or cerebellar hemispheres from 2 and 9 weeks of age (Fig. 2A). Hemotoxylin and eosin (H&E) stained sagittal sections revealed that cerebellar foliation and trilaminar organization were similar between *Slc25a46*$^{-/-}$ and WT mice (Fig. 2A). By 3 weeks of age, slight decreases in brain size and weight were found in mutant mice. A progressive decrease in size was noted after 6 weeks ($P < 0.01$), indicating progressive atrophy in the *Slc25a46*$^{-/-}$ mouse brain (Fig. 2B).

To investigate whether the smaller brain of *Slc25a46*$^{-/-}$ mice was associated with reduced proliferation or increased apoptosis, we performed immunohistochemistry (IHC) staining for cell
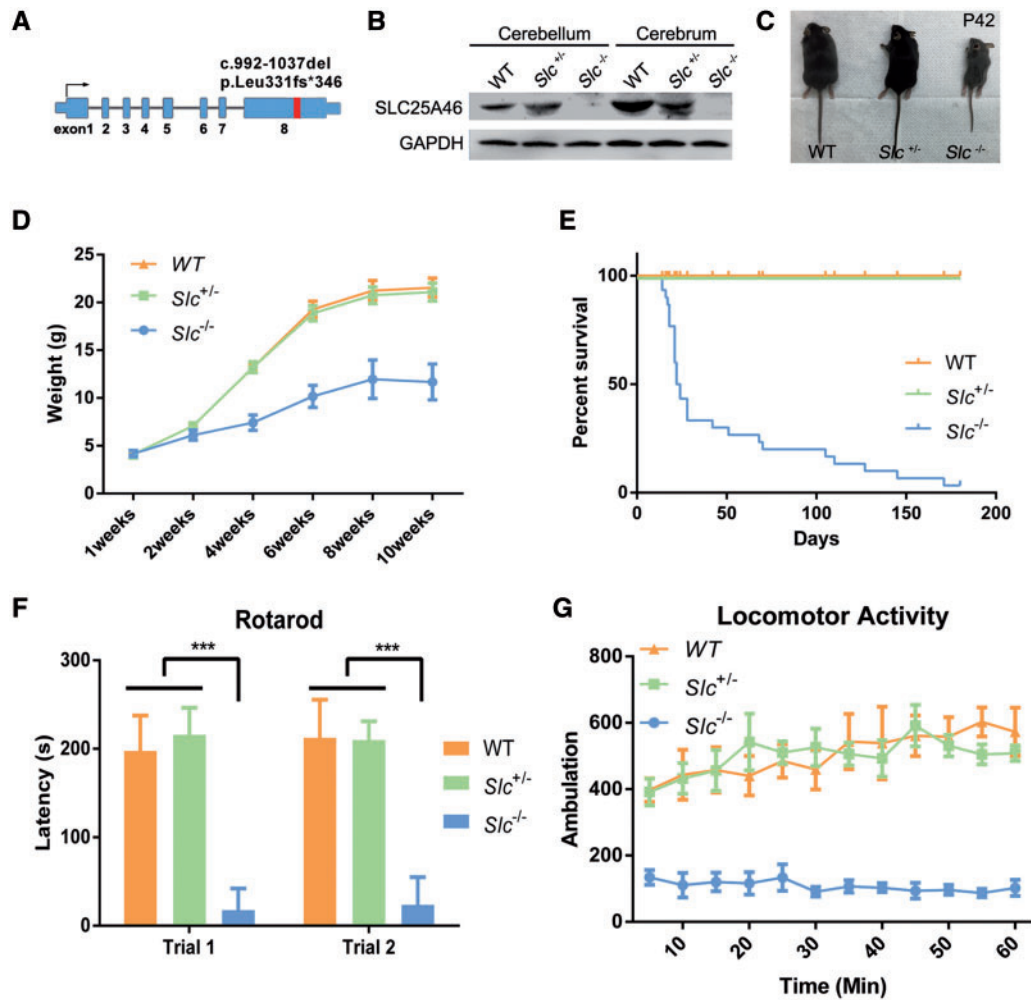
Figure 1. Delayed growth and impaired motor coordination of *Slc25a46* $^{-/-}$ mice. (**A**) Schematic map of *Slc25a46* with 46-bp deletion in exon 8. (**B**) Western blot analysis results of SLC25A46 protein expression in cerebrum and cerebellum. Loss of SLC25A46 was confirmed in *Slc25a46* $^{-/-}$ mice. (**C**) *Slc25a46* $^{-/-}$ mice exhibit growth deficiency at 6 weeks of age. (**D**) Weight measurement starting at P7. After P14, significantly decreased body weight was noted in *Slc25a46* $^{-/-}$ mice (P < 0.01; male, n = 8 for each group). (**E**) Kaplan-Meyer survival curve. Most SLC25A46 $^{-/-}$ mice died prematurely. Few mice survived beyond 6 months (P < 0.001; WT, n = 30; *Slc25a46* $^{+/-}$, n = 30; *Slc25a46* $^{-/-}$, n = 35). Survival curves were analyzed by Mantel–Cox test. (**F**) Rotarod test for 4-week-old female mice. (***P < 0.001; WT, n = 8; *Slc25a46* $^{+/-}$, n = 8; *Slc25a46* $^{-/-}$, n = 6). Results are combined from two independent tests. (**G**) Locomotor test revealed that 4-week-old *Slc25a46* $^{-/-}$ female mice exhibited reduced motor activity (P < 0.001; WT, n = 8; *Slc25a46* $^{+/-}$, n = 8; *Slc25a46* $^{-/-}$, n = 6). Activity was recorded every 5 min over a 60-min period.

proliferation marker phosphohistone H3 (PHH3) and apoptosis marker cleaved caspase-3 (CC3) respectively at P7, P14 and P42. No differences in these markers were identified in the cerebellum of *Slc25a46* $^{-/-}$ mice compared to their WT littermates (Supplementary Material, Fig. S2A showing P14 staining results).

To examine cell type-specific pathology in the *Slc25a46* $^{-/-}$ cerebellum, we performed histological analysis with several neuronal markers. Anti-NeuN was used to detect granule cells in the cerebellum. No obvious difference was found in the thickness of the granule layer between mutant and WT mice at P60, indicating a normal density of granule cells in *Slc25a46* $^{-/-}$ mice (Supplementary Material, Fig. S2B and C). Next, we performed immunofluorescence (IF) for Purkinje cells (PCs) using the specific marker calbindin. Results revealed loss of whole PCs or dendrites in *Slc25a46* $^{-/-}$ cerebellar sections (Fig. 2C). A decrease in calbindin staining (~20%) and remarkable PCs loss was

observed at P60 (P < 0.05), but there is no significant difference at P21 (Fig. 2D and E).

To confirm abnormal development of PC dendrites in the *Slc25a46* $^{-/-}$ cerebellum, we performed Golgi staining that can specifically visualize the intact morphology of neurons with dendrites and spines (29). In mutant mice, around 40% of stained PCs possessed only one or two primary dendritic branches with relatively straight extension in both directions at P30 and P60. In contrast, most WT PCs exhibited a highly stereotypic dendritic branching pattern, with 1 to 2 first-order branches emerging from the cell soma, followed by secondary and tertiary branches (Fig. 2F). This difference was found to be statistically significant (P < 0.001) (Fig. 2G).

We used magnetic resonance imaging (MRI) and spectroscopy to examine brain abnormalities in *Slc25a46* $^{-/-}$ mice. Brain volume measured by MRI again indicated a decrease in size, consistent with our analysis of the dissected brains (Supplementary
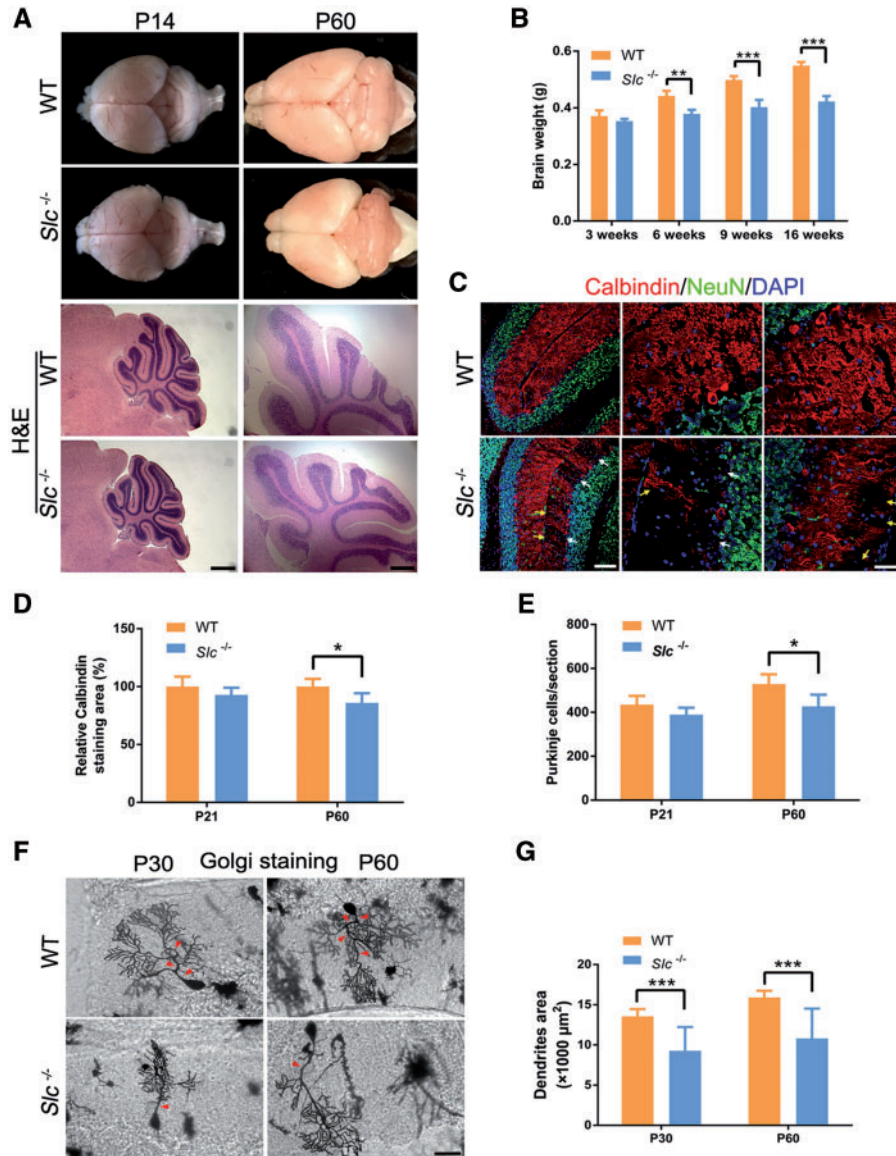
Figure 2. Purkinje cell loss and reduced dendritic branching. (**A**) Images of gross brains and H&E-stained mid-sagittal cerebellar sections. Scale bars: left bottom 2 images 800 µm; right bottom 2 images 200 µm. (**B**) Brain weight at different ages. (**P < 0.01, ***P < 0.001; WT control, $n = 4$; $SLC25A46^{-/-}$, $n = 4$ for 3, 6, 9 weeks; $n = 3$ for 16 weeks). (**C**) IF with calbindin staining. White arrows indicate loss of PCs. Yellow arrows indicate reduced dendrites. Scale bars: left 2 images 100 µm; right 4 images 40 µm. (**D,E**) Quantitation for calbindin staining (**D**) and Purkinje cell number per section (**E**) of P21 and P60 mice (*P < 0.05, 10 sections were measured from 3 mice for each group). (**F,G**) Golgi staining for P30 and P60 mouse cerebellum. Red arrowheads indicate primary dendrites (**F**). Area of dendrites was quantified (**G**) (***P < 0.001, 60-80 stained cells in 10 sections from 2 mice for each group were measured). Scale bars: 40 µm.

Material, Fig. S2D). *In vivo* MRI-guided spectroscopic analyses at 7T revealed a reduction of total N-acetylaspartate and N-acetylaspartylglutamate (tNAA) amounts in spectra acquired from $Slc25a46^{-/-}$ cerebellum compared to controls ($P < 0.05$), indicating metabolic abnormalities (Supplementary Material, Fig. S2E).

Purkinje cell loss is caused by cellular degeneration in $Slc25a46^{-/-}$ mice

As there was no significant difference in apoptosis staining in the central nervous system, one potential cause for the Purkinje cell loss and dendritic reduction could be neuronal degeneration. To assess neurodegeneration in $Slc25a46^{-/-}$ mice, brain

and spinal cord sections were stained with Fluoro-Jade C, a fluorescent high-resolution selective dye for neurodegeneration (30). Degenerative signals were present in axons, dendrites, and several somata of PCs in $Slc25a46^{-/-}$ mouse cerebellum at P60, but not in WT controls (Fig. 3A). Furthermore, toluidine blue-treated PCs somata and dendrites in $Slc25a46^{-/-}$ mice displayed dense staining, compared to WT. Some somata shrank into an irregular shape with dysmorphic stained dendrites in the molecular layer, indicating advanced stages of degeneration (31) (Fig. 3B). These findings were not evident in WT littermates and early age mutant mice at P30. Electron microscopic (EM) examination of the cerebellum confirmed the degeneration in axons, dendrites and somata of mutant PCs (Fig. 3A and B). Enlarged mitochondria with disorganized cristae, shrunk nucleus,
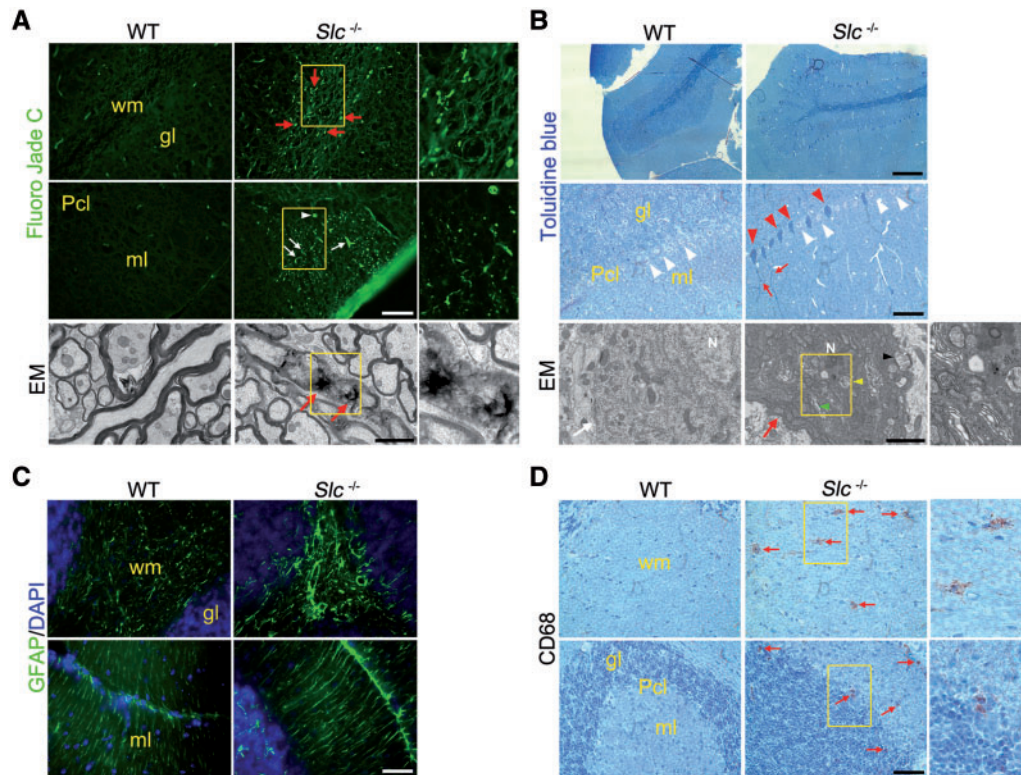
Figure 3. Neurodegeneration in $Slc25a46^{-/-}$ mouse cerebellum. **(A)** Fluoro-Jade C staining of PCs in mouse cerebellum. Red arrows indicate degenerating axons; White arrows indicate degenerating dendrites; White arrowheads indicate degenerating soma. EM confirmed degenerated axons (red arrows). wm: white matter; gl: granule layer; Pcl: Purkinje cell layer; ml: molecular layer. Scale bars: top 4 images 40 μm; bottom 2 μm. **(B)** Semithin (1–2s μm) resin sections stained with toluidine blue of PCs in mouse cerebellum. Red arrowheads indicate degenerating somata; Red arrows indicate dysmorphic dendritic arbors; White arrowheads indicate somata with normal morphology. EM confirmed high dense staining cells underlying degeneration (Red arrows indicate degenerated PCs; White arrows indicate normal PCs), in which enlarged mitochondria with disorganized cristae (black arrowhead), shrunk nuclei ("N"), autophagic vacuole (yellow arrowhead) and dilated endoplasmic reticulum (green arrowhead) were observed. Scale bars: top 160 μm; middle 40 μm; bottom 2 μm. **(C)** IF with GFAP staining in mouse cerebellum. Scale bars: 40 μm. **(D)** IHC with CD68 staining. Red arrows indicate positive signals. Yellow boxes indicate the enlarged regions. Scale bars: 40 μm.

autophagic vacuole and dilated endoplasmic reticulum were often found in degenerating PC bodies (Fig. 3B). Anti-myelin basic protein (MBP) and anti-adenomatous polyposis coli protein (APC), clone CC1 staining showed no obvious difference in the cerebellum white matter between $Slc25a46^{-/-}$ and WT mice, indicating that $Slc25a46$ mutation may not affect oligodendrocytes in the brain (Supplementary Material, Fig. S3A). Furthermore, neurodegenerative signals were also found in the vestibular nucleus of brainstem, deep cerebellar nuclei (DCN), striatum and corpus callosum of $Slc25a46^{-/-}$ mice, but not in other parts of brain, as well as presented in spinal cord (Supplementary Material, Fig. S3B).

Gliosis and inflammation are activated in response to degeneration or damage in the central nervous system. We performed IF staining for glial fibrillary acidic protein (GFAP) to detect gliosis. Enhanced GFAP expression was observed in the cerebellar white matter and molecular layer of $Slc25a46^{-/-}$ mice, suggesting the presence of activated gliosis (Fig. 3C). CD68 as an inflammatory marker was stained by IHC. Positive signals were observed in the cerebellar white matter and Purkinje cell layer of $Slc25a46^{-/-}$ mice, whereas these signals were absent in control littermates (Fig. 3D). Taken together, our results suggest that Purkinje cell neurodegeneration contributes to the pathogenesis of impaired motor coordination in $Slc25a46^{-/-}$ mice.

$Slc25a46$ mutation causes mitochondria dysmorphology and dysfunction in cerebellar neurons

To examine the mitochondrial morphology in affected cerebellum, ultrastructural analysis was performed by EM. In $Slc25a46^{-/-}$ PCs soma, we identified a portion of extremely enlarged mitochondria, which appear to be fused by a few mitochondria (Fig. 4A). We also noticed that mutant mitochondria in degenerative PCs were usually larger in diameter with vesiculation of their inner membranes, in contrast to the regular, accordion-like folds of cristae in WT mitochondria (Fig. 4A). Similar large round mitochondria with swollen cristae were also found in $Slc25a46^{-/-}$ PCs dendrites (Fig. 4B). They appeared to lose their polarity and distributed unevenly along the dendrites, frequently blocking at the dendritic intersections, which may restrict mitochondria from entering the distal, small branches (Fig. 4B). In contrast, the mitochondria of WT PCs have slender, tubule-like structures and generally fill the dendritic tracts in parallel (Fig. 4B). After quantitation, maximum diameter of mitochondria in mutant PCs dendrites was almost two-fold increased relative to WT dendrites (Fig. 4C).

Interestingly, in addition to the aberrantly large mitochondria, we also observed a remarkable increase of ring-shaped or C-shaped mitochondria in mutant PCs (usually in early stage of
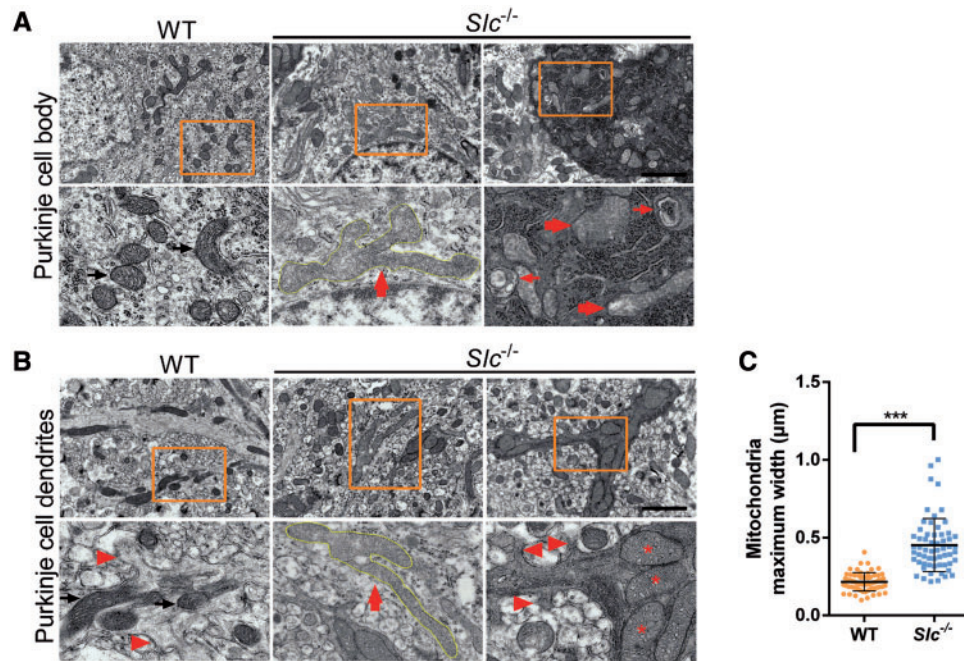
Figure 4. Enlarged mitochondria in *Slc25a46*$^{-/-}$ Purkinje cells. (**A**) EM of mitochondria in soma of PCs. Black arrows indicate normal mitochondria structure in WT. Thick red arrows indicate enlarged mitochondria, part of which appear to be the fusion of several mitochondria. Thin red arrows indicate mitochondria which may undergo mitophagy. Dark, dense cells indicate a degenerative cell body with shrunken shape. Scale bars: 2 μm. (**B**) EM of mitochondria in PC dendrites. Black arrows indicate slender, tubular mitochondria in small, WT PCs dendritic branches, which are close to the spines (Red arrowhead). Thick red arrow indicates enlarged mitochondria in *Slc25a46*$^{-/-}$ Purkinje cell dendrites. Asterisks indicate the congregation of large spherical mitochondria with swollen cristae at the dendritic intersection and are rarely found downstream around the spines. Scale bars: 2 μm. (**C**) Quantitation of maximum width of mitochondria in dendrites (***$P < 0.001$; 60 mitochondria from 10 images for each group were measured).

degeneration, recognized by light staining and smooth morphology of cell body), but in mutant granule cells mitochondria still kept normal (Fig. 5A). By examining multiple mitochondria in different *Slc25a46*$^{-/-}$ PCs, we inferred that the ring-shaped mitochondria were formed undergoing a series of changes. They may first compress and elongate from the middle, then bend around cytosolic constituents to form C-shape. Finally the head and the tail of such mitochondria fused together to form ring-shaped or spherical structure (Fig. 5B). They had typical mitochondrial features, including the double membranes although with disrupted cristae, and seemed to be different from autophagosomes.

Combination of dysmorphic mitochondria and disorganized cristae structure is often associated with compromised mitochondrial bioenergetics (32). To test the mitochondrial function, we isolated the mitochondria from the mouse cerebellum for the detection of complex activity and ATP production. Correspondingly, we observed significantly reduced activity levels of mitochondrial complexes I to IV ($P < 0.05$) in *Slc25a46*$^{-/-}$ mice, compared to WT mice (Fig. 5C). ATP production was also reduced by nearly 20% ($P < 0.05$) (Fig. 5D). These findings suggest *Slc25a46* mutations cause dysmorphic mitochondria and mitochondrial dysfunction in the neurons.

Improper distribution due to impaired transport of mitochondria during *Slc25a46*$^{-/-}$ neuron growth

To gain further insight into the roles of SLC25A46 function in maintaining physiological features of neurons, cerebellar neurons were isolated from P3 mice and cultured in vitro. At 5 days

in vitro (DIV), PCs were stained by calbindin and mitochondria were labeled with MitoTracker. Each cultured WT Purkinje cell displayed normal morphology with vase-like cell soma, extended axon and several dendrites (Fig. 6A). Mitochondria were evenly distributed in soma and dendrites (Fig. 6A). However, *Slc25a46*$^{-/-}$ PCs display dysmorphic soma with fewer dendrites. Swollen structures in dendrites and axons were easily observed in mutant PCs, suggestive of degeneration (33) (Fig. 6A). In addition, mitochondria frequently fused and aggregated in mutant PCs somata, but fewer mitochondria distributed in dendrites (Fig. 6A). Taken together with EM studies, these findings suggest that increases in the size of mitochondria likely impair transport of mitochondria along the dendrites in *Slc25a46*$^{-/-}$ PCs, thus leading to improper distribution. Thus we performed time-lapse imaging to test the real-time mitochondrial transport. During 4h time-lapse video, we found the movements of mitochondria in *Slc25a46*$^{-/-}$ PCs dendrites were slower than in WT PCs (Supplementary Material, Movie. 3 and 4). By using kymograph analysis, we studied mitochondrial dynamics modulations on mitochondrial mobility. We found that large and round mitochondria appeared to move much slowly. Some were even immobile in mutant dendrites (Fig. 6B). The velocity and path length were analyzed in both *Slc25a46*$^{-/-}$ and WT PCs, which were found a statistical significance between the two groups (Fig. 6C and D).

For C-shaped and ring-shaped mitochondria in vivo, it was reported that the changes are considered to occur in response to oxidative damage to mitochondria in cells (34,35). Therefore, we performed the ROS and superoxide assay in live cerebellar neurons. We found that indeed, ROS and superoxide level were increased in mutant neurons at 6 DIV by different probes
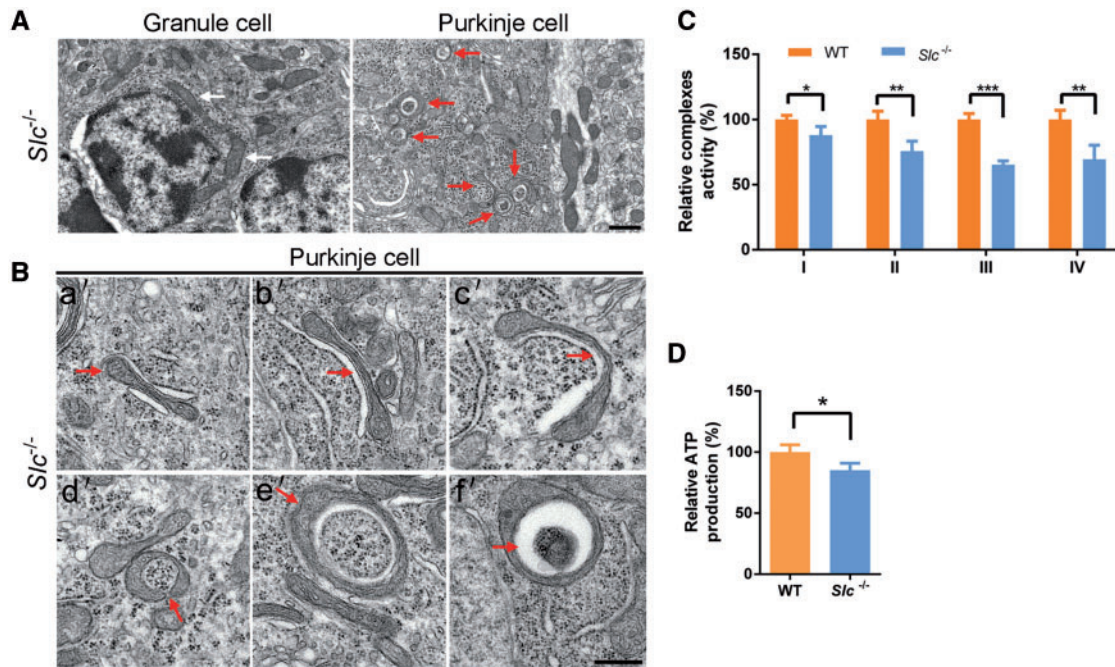
Figure 5. Ring-shaped mitochondria in *Slc25a46*$^{-/-}$ Purkinje cells and mitochondrial dysfunction in cerebellum. (**A**) EM of mitochondria in *Slc25a46*$^{-/-}$ granule cell and Purkinje cell. White arrows indicate mitochondria in *Slc25a46*$^{-/-}$ granule cell. Red arrows indicate C-shaped or ring-shaped mitochondria in *Slc25a46*$^{-/-}$ Purkinje cell at P30. Scale bars: 1 μm. (**B**) Different stages of ring-shaped mitochondria formation in *Slc25a46*$^{-/-}$ Purkinje cells at P30. (**a'**) Mitochondria elongated from the middle site. (**b'-d'**) Mitochondria bend around cytosolic constituents to form C-shape. (**e'**) Head and tail of individual mitochondria fused together to form ring-shape. (**f'**) Cytosolic constituents compressed and formed a vacuole in the center. Scale bars: 0.5 μm. (**C**) Mitochondrial enzymatic activity of respiratory chain complexes. Mitochondria were isolated from mouse cerebellum (*$P < 0.05$, **$P < 0.01$, ***$P < 0.001$; WT, $n = 4$; *Slc25a46*$^{-/-}$, $n = 4$). (**D**) ATP level in cerebellum (*$P < 0.05$; WT, $n = 4$; *Slc25a46*$^{-/-}$, $n = 4$). Data of (**C,D**) are representative of two independent replications.

(Supplementary Material, Fig. S4A and B). Autophagy was considered to be a response to oxidative damage (36). To examine autophagy in cerebellar neurons, we performed IF analysis to examine LC3 and ubiquitin, which are autophagosome markers. We found enhanced LC3 signals co-localized with enlarged mitochondria in *Slc25a46*$^{-/-}$ cerebellar neurons (Supplementary Material, Fig. S5A) and ubiquitin aggregated in degenerative dendrites of *Slc25a46*$^{-/-}$ PCs (Supplementary Material, Fig. S5B). These results support that *Slc25a46* is required for maintaining normal ROS and autophagy during neuron growth.

Slc25a46 mutation causes optic neuropathy in *Slc25a46*$^{-/-}$ mice

To investigate whether SLC25A46 deficiency in mouse can cause optic neuropathy, we analyzed the retina and optic nerves. Optical coherence tomography (OCT) as a noninvasive imaging technique was used to acquire cross-sectional tomographic images of the retina *in vivo* (37,38). Although images of the optic disc under bright field were grossly normal in terms of retinal appearance, OCT scanning revealed thinner retinas in aged *Slc25a46*$^{-/-}$ mice (Fig. 7A). Quantitative measurements indicated that the average thickness of the whole retina and ganglion cell complex (GCC), which includes the nerve fiber layer (NFL), ganglion cell layer (GCL), and inner plexiform layer (IPL), were decreased in *Slc25a46*$^{-/-}$ compared to control mice at P120 ($P < 0.05$; $P < 0.01$; respectively) (Fig. 7B). Outer retinal thickness was relatively normal. No significant difference was found in P30 mice, indicating an age-dependent process (Supplementary Material, Fig. S6A and B).

Retinal H&E-stained sections displayed normal organization of retinal structure but thinner inner retinas and noticeable retinal ganglion cell (RGC) loss in the GCL at P70 (Fig. 7C). Using the RGC marker Brn-3a for IF staining, we found that the number of Brn-3a–positive cells was reduced in *Slc25a46*$^{-/-}$ mice at P70 ($P < 0.001$), indicating degeneration of the RGCs (Fig. 7D). Although Brn-3a–positive cells were also slightly decreased at P30 ($P < 0.05$), no obvious loss of RGCs was found in H&E-stained sections (Supplementary Material, Fig. S6C and D). Semithin resin sections of toluidine blue-stained distal optic nerves of *Slc25a46*$^{-/-}$ mice at P30 and P60 displayed greater numbers of small axons compared to WT controls (Fig. 7E). EM examination at P60 showed that around 50% of axons were hypomyelinated in *Slc25a46*$^{-/-}$ optic nerves, with many unmyelinated and degenerating axons (Fig. 7E). In myelinated axons, G-ratio analysis (axon diameter divided by total fiber "axon + myelin sheath" diameter) indicated that the myelin thickness was decrease in *Slc25a46*$^{-/-}$ mice compared to controls ($P < 0.01$) (Fig. 7F). Diameters of most axons in *Slc25a46*$^{-/-}$ mice were smaller than WT littermates ($P < 0.001$) (Fig. 7G). Similar small axons were also found at P30 (Supplementary Material, Fig. S6E and F). Taken together, the data indicate that *Slc25a46*$^{-/-}$ mice display optic neuropathy associated with RGC loss and abnormal myelination associated with degeneration of optic nerves.

Slc25a46 mutation causes peripheral neuropathy associated with axon degeneration and demyelination

SLC25A46 mutations cause peripheral neuropathy in humans (1). Aged *Slc25a46*$^{-/-}$ mice displayed enhanced hind limb
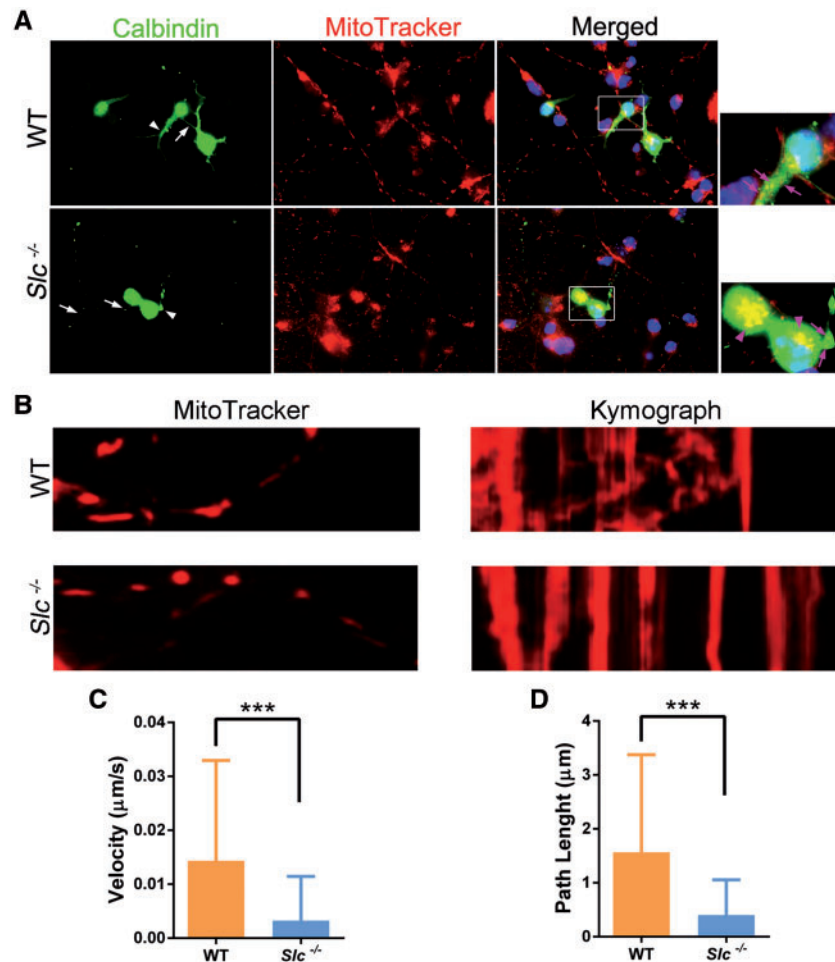
Figure 6. Affected mitochondria distribution and transport in *Slc25a46*$^{-/-}$ Purkinje cells. (**A**) Cultured cerebellar neurons at 5 DIV were stained with calbindin to identify PCs. Mitochondria were labeled by MitoTracker. White arrowheads indicate dendrites of PCs. White arrows indicate axons of PCs. Swollen structures were seen in mutant PCs dendrites and axons. Purple arrows in enlarged images indicate mitochondria in dendrites. Purple arrowheads in enlarged images indicate mitochondria in cell body. Scale bar: 40 μm. (**B**) Kymograph analysis of mitochondrial mobility in dendrites of PCs. Large, round mitochondria were seen in mutant dendrites. (**C,D**) Analysis of velocity and path length of mitochondria in PCs dendrites via time-lapse during 100s (***P < 0.001; More than 100 mitochondria in each group were measured).

clasping reflex and muscle atrophy, indicative of potential peripheral neuropathy (Fig. 8A). In many human peripheral neuropathies, demyelination is associated with muscle atrophy and lower extremity dysfunction. We examined peripheral nerve conduction in *Slc25a46*$^{-/-}$ mice by acquiring compound muscle action potentials (CMAPs) from the lateral gastrocnemius muscle during direct electrical stimulation of the exposed sciatic nerve *in vivo*. Based on recorded electromyography (EMG) wave (Fig. 8B), conduction velocity (CV) and CMAP amplitude were measured. CVs and CMAP amplitudes were decreased in P60 *Slc25a46*$^{-/-}$ mice (P < 0.001) compared to normal littermates, suggestive of possible myelination defects (Fig. 8C and D).

To examine myelination in the peripheral nervous system, sciatic nerves of *Slc25a46*$^{-/-}$ mice were collected for toluidine blue staining and electron microscopic (EM) examination. Semithin resin sections of toluidine blue-treated nerves from P30 and P60 showed slight global hypomyelination in *Slc25a46*$^{-/-}$ mice (Fig. 8E; Supplementary Material, Fig. S7 for P30). EM of sciatic nerves from *Slc25a46*$^{-/-}$ mice at P60 confirmed that greater than 40% of axons were hypomyelinated, with a portion

of axons showing degeneration and demyelination (Fig. 8E). In myelinated axons, analysis of the G-ratio showed a decrease in myelin thickness in *Slc25a46*$^{-/-}$ mice (P < 0.001) (Fig. 8F). Diameters of approximately 80% of *Slc25a46*$^{-/-}$ axons were in the range of 1 to 4 μm, which is remarkably smaller in size compared to WT controls (P < 0.001) (Fig. 8G). These results, combined with positive Fluoro-Jade C staining in the spinal cord (Supplementary Material, Fig. S3B), indicate that peripheral neuropathy is caused by peripheral axon degeneration and demyelination.

By ultrastructural study, we identified a portion of aberrantly enlarged mitochondria, which tended to clump together, in mutant sciatic nerves (Fig. 8H). Vesicular-like or loss of cristae were noticed in mutant mitochondria, in contrast to the regular, accordion-like folds of cristae in WT mitochondria (Fig. 8H). Occasionally, a cluster of messy mitochondria were observed in degenerating axons (Fig. 8H). Quantitative measurements of the mitochondrial diameter indicated mitochondrial size in *Slc25a46*$^{-/-}$ mice was notably larger than WT mice (P < 0.001) (Fig. 8I).
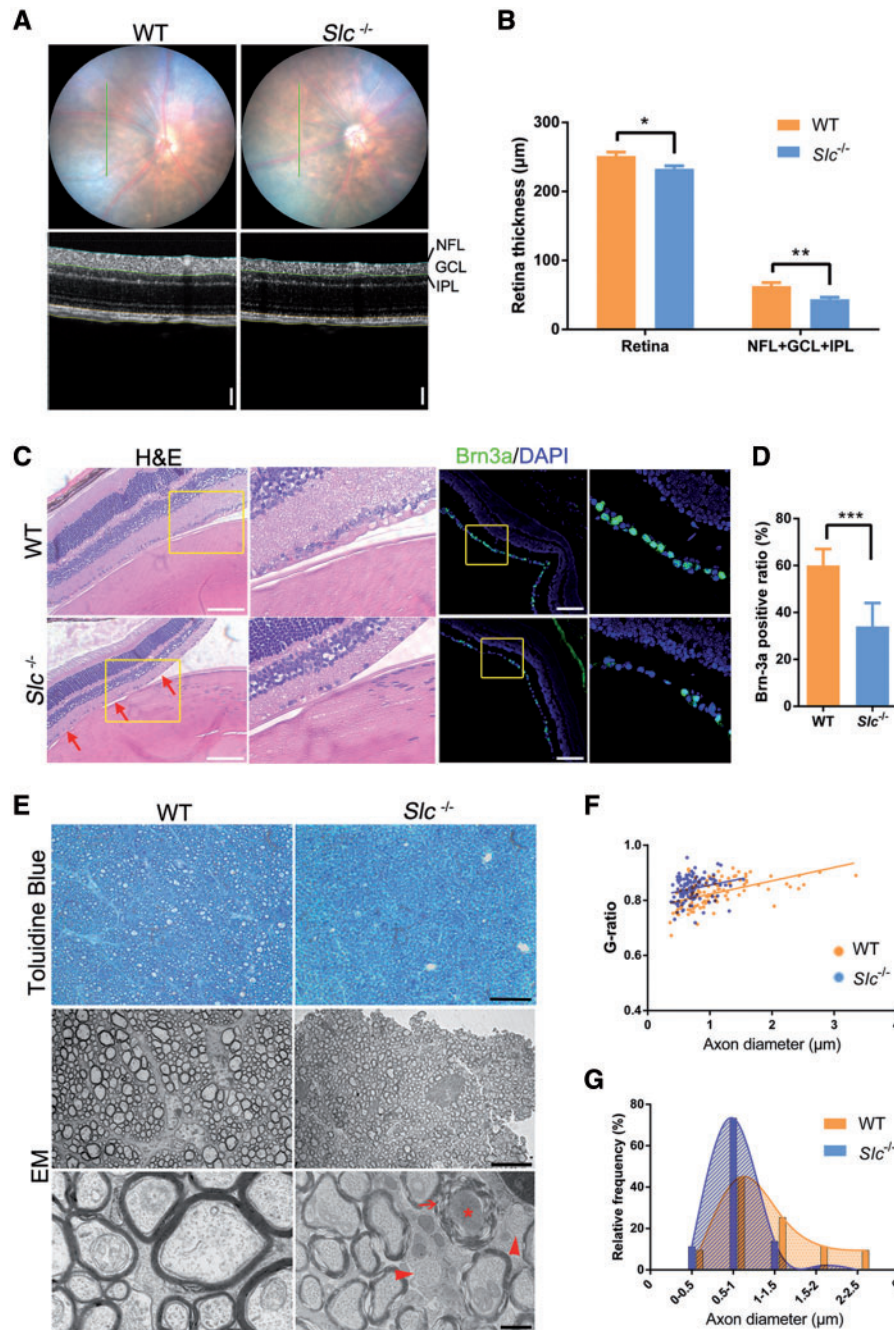
Figure 7. RGC loss and optic nerve demyelination and degeneration. (**A**) Optic disc and OCT scanning of P120 mice. Green line in optic disc images indicates position of OCT scanning. Scale bars: 63 μm. (**B**) Quantitation for retinal thickness from OCT scanning images (*$P < 0.05$, **$P < 0.01$; $n = 3$ for WT and $Slc25a46^{-/-}$ mice). (**C**) H&E and Brn-3a staining for retinas. Scale bars: 100 μm. (**D**) Quantitation of Brn-3a–positive RGCs in retinas of P70 mice (***$P < 0.001$, Brna-3a–positive RGCs were counted from six retinal sections of P70 mice) ($n = 3$ for WT and $Slc25a46^{-/-}$ mice). (**E**) Toluidine blue-stained semithin cross-sections and EM images of P60 optic nerves. Arrowheads indicate unmyelinated axons. Asterisk indicates degenerative axon underlying demyelination (arrow). Scale bars: top 20 μm; middle 8 μm; bottom 0.5 μm. (**F**) Scatterplot displays G-ratios of individual optic nerve axons ($P < 0.01$, data collected from 100–300 myelinated fibers per group; $n = 3$ for WT and $Slc25a46^{-/-}$ mice). (**G**) Distribution of axon diameters for optic nerves ($P < 0.001$; $n = 3$ for WT and $Slc25a46^{-/-}$ mice).

Discussion

In mice, most of the homozygous mutants for mitochondrial dynamics-related genes, like *Mfn2*, *Opa1*, and *Drp1*, are embryonic lethal, while heterozygous mutants or conditional knock-out mice usually show pathological changes in unitary tissue (23,39–42). Nevertheless, $Slc25a46^{-/-}$ mouse had a grossly normal embryonic development and recapitulated most of the human phenotypes, with multiple progressive neuropathies as well as retarded growth. Based on this mouse model, we discovered underlying cellular lesions in affected nervous tissues by histopathological analysis.

Movement disorder was presented in almost all of reported patients, but the onset of this phenotype varied, which might be
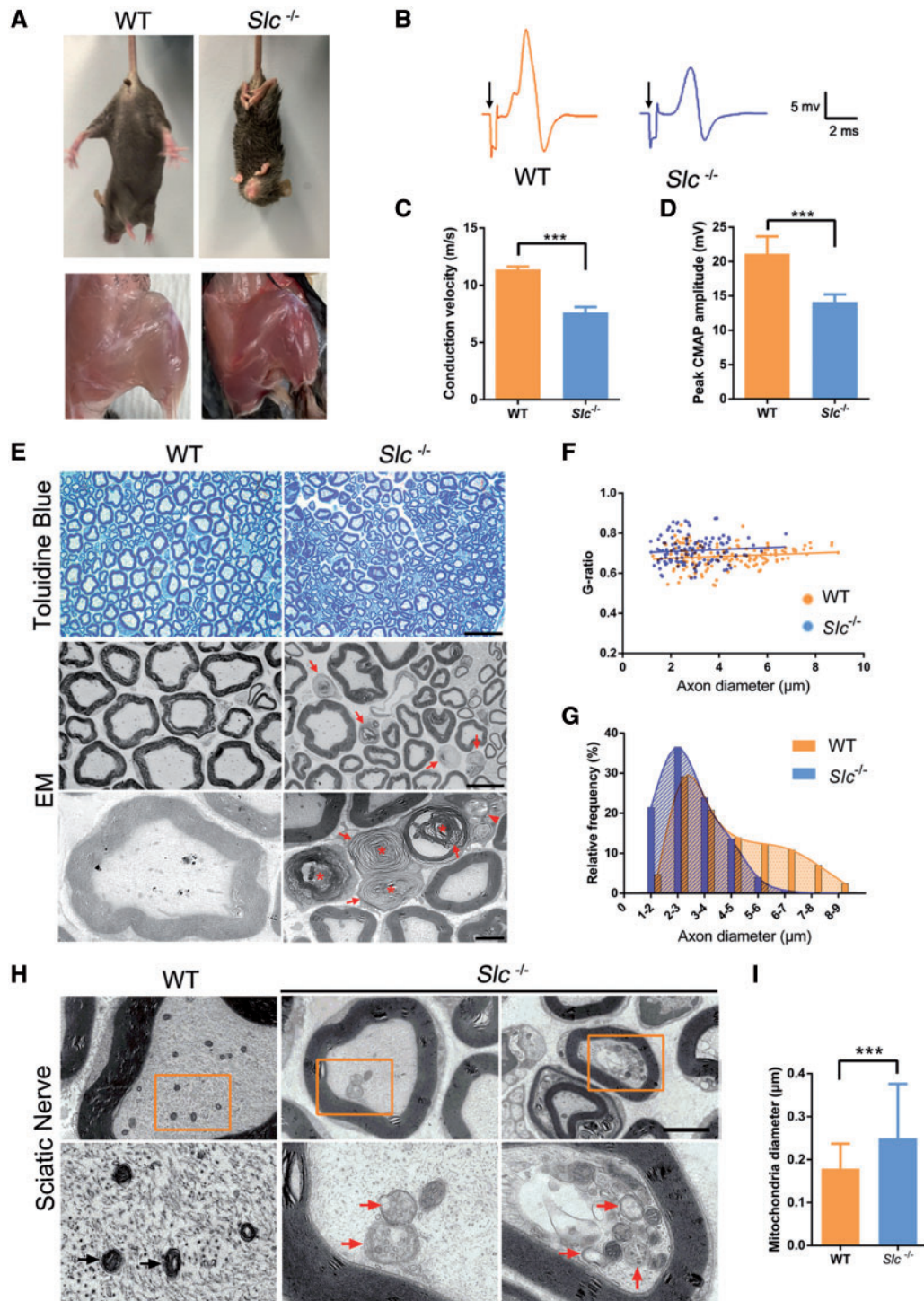
Figure 8. Peripheral neuropathy with axon degeneration and demyelination in *Slc25a46*$^{-/-}$ Mice. (**A**) When lifted by the tail, enhanced limb-clasping reflex was presented in *Slc25a46*$^{-/-}$ mice compared to WT mice at P60 (Top). Representative images showing hindlimb muscle atrophy in *Slc25a46*$^{-/-}$ mice at P120 (Bottom). (**B-D**) CMAP recordings of P60 sciatic nerve. CVs (**C**) and CMAP amplitudes (**D**), measured from recorded waves (**B**) (Arrows indicate onset of electrical stimulation of the sciatic nerve during recording) ($n = 4$ for WT and SLC25A46 $^{-/-}$ mice; $P < 0.001$). Data are representative of two independent experiments. (**E**) Toluidine blue-stained semithin cross-sections and EM images of P60 WT and *Slc25a46*$^{-/-}$ sciatic nerves. Asterisks, degenerative axons; Arrows, demyelination; Arrowhead, autophagy. Scale bars: top 20 μm; middle 8 μm; bottom 2 μm. (**F**) Scatterplot displaying G-ratios of individual sciatic nerve axons ($P < 0.001$, data collected from 100–300 myelinated fibers per group; $n = 3$ for WT and *Slc25a46*$^{-/-}$ mice). (**G**) Distribution of axon diameters for sciatic nerves ($P < 0.001$, data collected from 100–300 myelinated fibers per group; $n = 3$ for WT and *Slc25a46*$^{-/-}$ mice). (**H**) Mitochondria in WT peripheral axon showed small size and even distribution (black arrow). Mitochondria often clumped together with disorganized cristae or loss of cristae (red arrow) in mutant mice. Scale bars: 2 μm. (**I**) Quantitation for mitochondrial diameter (***$P < 0.001$, data collected from 200-300 mitochondria per group; $n = 3$ for WT and *Slc25a46*$^{-/-}$ mice).

due to the different mutant genotype of *SLC25A46*. Our *Slc25a46*⁻/⁻ mice displayed visible ataxia and balance issues at 2 weeks postnatal and became progressively worse. Based on the results of anatomical and histological analyses, cerebellar atrophy with specific loss of PCs could be the primary cause of severely impaired motor coordination. Degeneration in Purkinje cells is the major cause of neuron loss. Similarly to mice with conditional knock-out *Mfn2* or *Drp1* mutations, *Slc25a46*⁻/⁻ mice showed major changes in cerebellar PCs, whereas granule cells seemed to be spared (40). We have yet to determine why some neurons are selectively affected by abnormal mitochondrial function and dynamics. One possibility is that the Purkinje cell is one of the largest neurons in the brain, with a relatively long axon and extremely extensive dendritic branches. This type of neuronal architecture requires the proper transport and distribution of highly organized organelles, such as mitochondria.

When we examined the cerebellum using EM, aggregation of enlarged and spherical mutant mitochondria with swollen cristae were often visualized at dendritic intersection and were rarely found around the spines, resulting in poor mitochondrial distribution in PC dendrites. After further tests in cultured mutant PCs, we confirmed that impaired motility likely underlies the paucity of mitochondria in neurites. As poor mitochondrial distribution could cause insufficient ATP production and Ca^{2+} buffering in the termini (43), ultimately leading to the death of dendrites, axons, and then cell bodies of neurons, this could be the underlying pathogenesis of mutant PC loss and dendritic abnormalities. These findings further confirm the role of SLC25A46 in mitochondrial dynamics. Although our previous study suggested that SLC25A46 may function as a pro-fission factor (1), other subsequent studies based on non-neuron cell models showed that SLC25A46 may mediate mitochondrial dynamics by regulating contacts between the endoplasmic reticulum (ER) and mitochondria or serves as a regulator for MFN1/2 oligomerization (3,6). Thus, the molecular mechanism of SLC25A46 function remains elusive and needs to be further studied. Given the central metabolic function of mitochondria, mitochondrial dynamics and bioenergetics reciprocally influence each other (44). Our results support the notion that fusion/fission imbalance in *Slc25a46*⁻/⁻ mice cerebellum is associated with a reduction in respiratory complex activities and ATP production, indicative of cellular metabolic dysfunction.

According to several studies, a ring-shaped mitochondrial morphology may be indicative of a cellular response to oxidative damage in the mitochondria (34,35). We identified C-shaped or ring-shaped mitochondria and increased ROS levels in our mutant cerebellar neurons, suggesting that antioxidants could be an option for treatment as shown in *Drp1*KO Purkinje cells (25). Our results also support the conclusion that neurons with a high level of ROS require balanced mitochondrial dynamics to reduce oxidative damage (45–47). Otherwise, autophagy is needed to eliminate accumulated damage to mitochondria, which is consistent with our findings that increased level of the autophagy marker LC3B colocalized with large mitochondria in mutant neurons.

Optic atrophy is one of the striking phenotypes in human patients with SLC25A46 mutations. By histological analysis in *Slc25a46*⁻/⁻ mice, RGC degeneration was found to be the major pathological feature of SLC25A46-related optic atrophy. Due to the severely impaired motor coordination of *Slc25a46*⁻/⁻ mice, we were unable to examine visual acuity by slit-lamp tracking. However, our results revealed significantly reduced retinal and GCL thicknesses in adult *Slc25a46*⁻/⁻ mice, associated with RGC and optic nerve degeneration and unmyelination. The hallmark of ADOA is the preferential involvement of small fibers with abnormal myelination (41). *Slc25a46*⁻/⁻ mice revealed very similar features. One plausible explanation is that the thin fibers in *Slc25a46*⁻/⁻ may have compromised transport of the hyperfused mitochondria.

EMG of the sciatic nerves in adult *Slc25a46*⁻/⁻ mice showed reduced CAMPs and CVs, which was further supported by EM observations that the distal sciatic nerves display hypomyelination with degeneration and demyelination in axons. In general, this change was not as severe as the changes in CMT1, which are usually caused by dysfunction of myelin-related proteins such as PMP22 and MPZ. In those cases, general segmental demyelination and remyelination ("onion bulbs") are more obvious (48,49). In *Slc25a46*⁻/⁻ mice, dysmorphic mitochondria were also prominent and mainly found in axons, but not in SCs, providing the pathological evidence that the peripheral neuropathy was of the axonal CMT (CMT2) subtype. The reduction of CV in *Slc25a46*⁻/⁻ mice could be secondary to demyelination, which results from axon degeneration induced by abnormal mitochondria dynamics as a primary cause.

Together with the degeneration in long peripheral axons and distal optic nerves of *Slc25a46*⁻/⁻ mice, our results support that neurons with long axons or complicated dendrites are more sensitive to abnormal mitochondrial dynamics. Similar to the findings in *Slc25a46*⁻/⁻ Purkinje cells, this sensitivity also could be due to the impaired mobility and transport of *Slc25a46*⁻/⁻ hyperfused mitochondria along the axons and dendrites, probably due to their abnormal size and/or reduced ATP availability in the distal portion of long axons secondary to mitochondrial dysfunction. Further studies will be needed to clarify this point.

In conclusion, our *Slc25a46* knock-out mouse model recapitulates most of the phenotypes in patients. This model allows us to study multiple neuropathies *in vivo*, including ataxia, peripheral and optic neuropathies. Our findings support a model in which *Slc25a46* mutations cause abnormal mitochondrial morphology and dysfunction, thereby potentially altering mitochondrial transport and distribution in the long axons and extensive dendrites. These energy deficiencies in the distal axons and synaptic terminals and abnormal mitochondrial dynamics lead to neurodegeneration and demyelination and cause cell body degeneration in a retrograde fashion. This mouse model provides an incredibly valuable tool to investigate the pathophysiology of neuropathies and mitochondrial dynamics *in vivo*. Understanding the cellular pathogenic mechanisms of *SLC25A46* mutations will open new avenues to developing effective treatments for the mitochondrial dynamics-related diseases, including many common neurodegenerative diseases.

Materials and Methods

Generation of *Slc25a46*⁻/⁻ mice

Multiple sgRNAs targeting exon 8 of *Slc25a46* were designed using the CRISPR Design Tool website (http://crispr.mit.edu:8079/?). To improve editing activity, we modified the pX458 vector (Addgene #48138) by flipping an A-T base pair and extending the Cas9-binding hairpin structure to create a pX458M vector (50). The sgRNA target sequence was cloned into pX458M. Editing activity was validated by the T7E1 assay in mK4 cells (51), compared side-by-side with Tet2 sgRNA that was previously published and known to work (52). Validated sgRNA (5'-TGACGTTATA CTTTACCCAC-3') and Cas9 mRNA were transcribed *in vitro* and

injected into the cytoplasm of fertilized eggs of B6D2F2 genetic background. Injected eggs were transferred into the oviductal ampulla of pseudopregnant CD-1 females. Pups were born and genotyped by PCR with the following primer pair: forward, 5'-ACGAGTGATA GGCTTGGGAG TG-3'; reverse, 5'-ACCAAACACT CCTTCCTCCT GC-3'. Offspring were genotyped by genomic PCR and Sanger sequencing. Animals were housed in a controlled environment with a 12-h light/12-h dark cycle, with free access to water and a standard chow diet. Diet gel (DietGel® 76A, ClearH$_2$O) was provided to affected homozygous mice. Unaffected littermates and WT mice were used in the experiments as controls. All animal procedures were carried out in accordance with the Institutional Animal Care and Use Committee-approved protocol of Cincinnati Children's Hospital and Medical Center.

Western blot

Western blot analysis was performed as described (53). Rabbit anti-SLC25A46 N-terminal (1:1,000, Aviva Systems Biology) and mouse anti-GAPDH monoclonal antibody (1:4,000, Ambion) was applied.

Behavioral studies

Motor coordination and balance were assessed with a rotarod test. Each mouse was placed on the rotating drum of an accelerating rotarod (UGO Basile Accelerating Rotarod, OH) at increasing rates from 4 to 40 rpm over a 3-min period. The time that each mouse was able to maintain its balance on the rod was determined as the latency time to fall (s).

Locomotor activity was measured in a $41 \times 41 \times 30$ cm Accuscan activity monitor equipped with 16 pairs of photodetector-LED beams along the x and y axes (Accuscan Electronics with VersaMax Software, OH). The test was conducted under normal overhead fluorescent lighting. Individual mice at 4 weeks were placed in the chambers for 60 min. Total ambulation activity was recorded in 5-min intervals.

Histological procedures

Frozen tissue sections were processed as described (54). Briefly, mice were perfused transcardially with PBS and fresh 4% paraformaldehyde (PFA) in PBS. After overnight postfixation in 4% PFA at 4 °C, tissues were incubated in 30% sucrose for at least 24 h. Paraffin sections (5–8 μm in thickness) were cut and processed for immunocytochemistry according to an avidin/biotin amplification protocol using diaminobenzidine (DAB) as chromogen and H&E staining. Cryosections (12–20 μm in thickness) cut on a cryostat (LEICA CM1850) were processed for IHC or IF. Sections were labeled with the following primary antibodies: rabbit anti-CC3 (1:300, Cell Signaling), rabbit anti-phosphohistone H3 (1:50, Sigma), mouse anti-NeuN (1:2,000, Millipore), rabbit anti-calbindin D28k (1:1,000, Swant), mouse anti-GFAP (1:1,000, Millipore), rat anti-CD68 (1:200, Abcam), goat anti-MBP (1:500, Santa Cruz), goat anti-CC1 (1:500, Millipore), rabbit anti-Brn-3a (1:250, Santa Cruz). Secondary antibodies from goat or donkey were conjugated to biotin (1:200, Jackson ImmunoResearch), Alexa Fluor-488, -549, or cyanine 5 (1:500, Jackson ImmunoResearch). Processed sections were mounted onto SuperFrost microscope slides (Menzel-Glaser) by using mounting medium with DAPI (Vector) and imaged with Zeiss Axiovert 200M microscope or Nikon C2 confocal microscopes. Quantification of Purkinje cell staining was performed by using ImageJ software (National Institutes of Health) or NIS elements (Nikon).

Golgi staining

After mice were deeply anesthetized, the cerebellum was quickly removed and prepared for Golgi staining using the FD Rapid Golgi Stain Kit (FD NeuroTechnologies) according to the manufacturer's protocol. After staining, the cerebellum was embedded in 4% agarose and cut into 150-μm sagittal section by vibratome (LEICA VT1000 S). The sections were then mounted on slides, dehydrated with xylene and then cover-slipped with permount (Fisher Scientific). Images were acquired with Zeiss Axioskop and quantified using ImageJ software (National Institutes of Health).

Fluoro-Jade C staining

Sections were mounted on gelatin-coated slides, air-dried, and subjected to Fluoro-Jade C staining. Slides were immersed in a solution containing 1% NaOH in 80% ethanol for 5 min, rinsed in 70% ethanol for 2 min, rinsed in distilled water for 2 min, and incubated in 0.06% potassium permanganate solution for 10 min. Following a water rinse for 2 min, slides were transferred to 0.0001% Fluoro-Jade C staining solution dissolved in 0.1% acetic acid for 10 min. After three washings with water, slides were air-dried on a slide warmer at 50 °C for 30 min, then cleared in xylene and cover-slipped with DPX (Sigma-Aldrich). Signals were visualized with a Zeiss Axiovert 200M microscope.

In vivo MRI and spectroscopy

Data were collected on a Bruker BioSpec 7-T system (Bruker BioSpec 70/30, Karlsruhe, Germany) equipped with 400 mT/m actively shielded gradients and Paravision 6.0 software. Animals were anesthetized by 1% to 2% isoflurane delivered by oxygen. Respiration rate was maintained at around 80 breaths per minute. Animals were kept warm with a flow of warm air controlled by a Small Animal Instruments (Small Animal Instruments, Inc., Stony Brook, NY) monitoring system. Mice were centered in a home-build 25 mm ID solenoid coil. Localizers were acquired in all three planes, followed by an ungated 3D RARE sequence (repetition time 1.2 s, effective echo time 56 ms, 0.2 mm isotropic resolution) for volumetric measurements. PRESS spectra (repetition time 2.5s, echo time 20 ms) were acquired from a $2 \times 2 \times 4$ mm voxel in the thalamus and a $1.5 \times 1.5 \times 1.5$ mm voxel in the cerebellum. Total scan time was about 1 h. Volumes were estimated by drawing regions-of-interest in ImageJ. MRS data were quantified using the LCModel software with water as an internal reference (55).

Electron microscopy

Mice were anesthetized and perfused with 0.9% NaCl and EM fixative (4% paraformaldehyde, 2.5% glutaraldehyde, PBS, pH 7.4–7.6). Tissues were postfixed in EM fixative buffer, washed in 0.1 M Na cacodylate buffer (EMS, Hatfield, PA), and postfixed in 1% osmium tetroxide (EMS) for 1 h at 4 °C. Samples were washed in 0.1 M Na cacodylate buffer and dehydrated through a graded ethanol series. Samples were embedded in LX-112 (Ladd Research Industries, Williston, VT). Tissue blocks were sectioned to a thickness of 0.5 to 1 μm and stained with toluidine blue for light microscopic examination. Blocks were cut and

trimmed with an ultramicrotome (Leica EM UC7, Buffalo Grove, IL) to 90-nm thickness. Sections were counterstained with uranyl acetate 2% (EMS) and lead citrate. All images were taken with an 80-kV transmission electron microscope (Hitachi, H-7650, V01.07, Tokyo, Japan). Mitochondria width or diameter, axon and myelin thickness were quantified by ImageJ software (National Institutes of Health)

Complex activity

Activities of respiratory chain complexes were determined as described previously (56). Briefly, complex I activity was assessed by measuring the decrease of NADH absorbance at 340 nm, using decylubiquinone as an electron acceptor. Complex II activity was measured by following the reduction of 2, 6-dichlorophenolindophenol (DCPIP) with the decrease of the absorbance at 600 nm of oxidized DCPIP. Complex III activity was determined by measuring the reduction of cytochrome c by an increase of absorbance at 550 nm. Complex IV activity was measured by monitoring the oxidation of reduced cytochrome c as a decrease of absorbance at 550 nm (Cary 300 UV-Vis Spectrophotometer Agilent, CA). Activities of complexes I to IV were normalized by citrate synthase activity and used in the analysis.

ATP production

ATP Bioluminescence Assay Kit CLS II was used for the ATP assay according to the manufacturer's instructions (Roche Applied Science). Cerebellum from mice were minced into 1- to 2-mm^3 pieces in ice-cold isolation buffer (10 mM EDTA/0.05% trypsin in phosphate-buffered saline, PBS), incubated for 30 min on ice, and centrifuged at $300 \times g$ for 5 min. Harvested pellets were homogenized in ice-cold PBS containing 10 mM EDTA and protease inhibitor using the GentleMACS Dissociator. Homogenized samples were filtered with 70-μm filters and centrifuged (4 °C, 5 min at $800 \times g$). Resultant supernatants were used to detect ATP levels. Assay buffer and substrate were equilibrated to room temperature, and buffer was transferred to and gently mixed with the substrate to obtain a homogeneous solution. After equilibration, 100 μl of the assay reagent and 100 μl of tissue lysis buffer were added to each well. Luminescence was read on a microplate reader (Synergy H1, Bio-Tek).

Cerebellar neuron culture and immunofluorescence

Cerebellar neurons were isolated and cultured according to the methods described in previous reports (25,57). Briefly, after genotyping for the newborn mice, cerebella from P3 mice were dissected and dissociated by Papain Dissociation System Kit (Worthington Biochemical Corporation). Cerebella were incubated with 20 units/ml papain in EBSS for 20 min at 37 °C. After three washings with EBSS, cerebella were dissociated by pipetting ten times each with a regular Pasteur pipette and a fire-polished Pasteur pipette coated with fetal bovine serum. The cell suspensions were transferred into a fresh tube and centrifuged at 200g for 5 min at room temperature, then resuspended in 200 μl of inhibitor solution (100 μg/ml ovomucoid inhibitor, 100 μg/ml albumin, 10 U/ml DNaseI in EBSS). Cells were collected by centrifugation at 200g for 5 min at room temperature and resuspended in seeding medium (100 μM putrescine, 30 nM sodium selenite, 1% penicillin–streptomycin, in DMEM/F12) supplemented with 10% fetal bovine serum. $1.5–2 \times 10^5$ cells were plated onto each 3.5-cm coverslip-bottomed dish (P35G-0-14-C; MatTek), which was coated with 1 mg/ml poly-L-lysine in 100 mM borax buffer, pH 8.5, at 37 °C for 2 d. After the neurons were incubated at 37 °C for 3 h, 2.3 ml of seeding medium supplemented with 1% penicillin–streptomycin, 3.9 mM glutamine, 2.1 mg/ml glucose, 200 μg/ml transferrin, 40 nM progesterone, 20 μg/ml insulin, 0.5 ng/ml triiodothyronine, 100 μg/ml bovine serum albumin, and 5% fetal bovine serum were added to the dish. Half of the culture medium was replaced with seeding medium every 2–3 days.

500 nM MitoTracker® Red CM-H2XRos (M7513, Invitrogen) was used to label mitochondria in live cells (and can be retained after fixation). For immunofluorescence, cerebellar cells were fixed in pre-warmed 4% paraformaldehyde in PBS for 20 min, washed with PBS three times, and permeabilized with 0.1% Triton X-100 in PBS for 10 min. After blocking in PBS containing 0.5% BSA and 10% donkey serum, cells were incubated overnight at 4 °C with antibodies to calbindin D28k (1:1000, Swant), Tom20 (1:500, Millipore), LC3 (1:500, Cell Signaling Technology), and ubiquitin (1:500, BD Bioscience), followed by the appropriate secondary anti-bodies. Cells were viewed using Zeiss Axiovert 200M microscope or Nikon C2 confocal microscopes.

Time-lapse imaging

For time-lapse imaging of the mitochondria, live cerebellar neurons were labeled with MitoTracker® Red CM-H2XRos (M7513, Invitrogen) and monitored by an incubator microscope (Nikon SpectraX wide field) equipped with a 60× objective (NA = 1.40, Nikon) at 5s intervals for 4h. Kymograph, velocity and path length of the mitochondria in dendrites were analyzed and quantified by NIS elements software (Nikon).

ROS and superoxide assay

Levels of ROS were detected with ROS/Superoxide Detection Assay Kit (Abcam). Briefly, cerebellar neurons were seeded into three groups as negative, positive and testing group. Negative control cells were treated by 30 min with the ROS inhibitor (N-acetyl-Lcysteine). Pyocyanin was then added into both negative and positive control cells to induce ROS and superoxide. To measure ROS and superoxide production, all 3 groups of cells were incubated with the oxidative stress detection reagent (green) and superoxide detection reagent (orange) for 30 min to 1 h. Subsequently, cells were washed twice with 1X a Wash buffer. After fluorescence calibration by negative and positive groups, cell images were captured under Zeiss Axiovert 200M microscope using standard excitation/emission filter sets (green 490/525 nm and orange 550/620 nm).

Compound muscle action potential (CMAP) recording

Mice were first anesthetized with an intraperitoneal injection of 50 mg/kg sodium phenobarbital. The lateral gastrocnemius muscle was then exposed from the knee to about 4 mm above the ankle. Sciatic nerve was exposed near the biceps femoris muscles. Mylar-coated steel recording wires (California Fine Wire) were implanted into the lateral gastrocnemius muscles, and reference wires were inserted under the skin near the base of the tail. A concentric bipolar stimulating electrode was placed on the sciatic nerve and used for electrical activation.

CMAPs were amplified, obtained with a Micro 1401 data acquisition unit, and analyzed offline with Spike2 software

(Cambridge Electronic Design, Cambridge, UK). A 2- to 4-mA electrical stimulation of the sciatic nerve immediately proximal to the tibial, sural, and common peroneal branches was employed via a stimulus isolation unit (WPI) connected to the Micro 1401. After recording, the sciatic nerve was axotomized. The proximal end of the sciatic nerve was stimulated to ensure that CMAPs were generated from direct nerve stimulation. CMAP CV, amplitude, and duration were calculated from each stimulation paradigm. The average stimulation of the sciatic nerve for each paradigm was obtained and averaged across animals.

In vivo imaging using OCT

Mice at P30 and P120 were anesthetized with a mixture of xylazine (6 mg/kg) and ketamine (100 mg/kg). Pupils were dilated with a topical drop of cyclomydril (Alcon Laboratories, Fort Worth, TX). Two minutes after pupil dilation, lubricating eye drops (Alcon Laboratories) were applied to the cornea. Spectral domain OCT with guidance of bright-field live fundus image was performed using the image-guided OCT system (Micron IV, Phoenix Research Laboratories) according to the manufacturer's instructions. The vendor's image acquisition software was used to generate fundus images and OCT scans. The vendor's software (Insight) was used to measure thicknesses of retinal layers (NFL + IPL + INL) and entire retinas.

Statistical analysis

Results are presented as means ± SD. Graphical illustrations and significance were obtained with GraphPad Prism 5 (GraphPad) using Student's t test or multiple comparison ANOVA, followed by Bonferroni or Dunnett post hoc tests (according to the sample sets), unless otherwise stated. $P < 0.05$ was considered statistically significant ($^*P < 0.05$; $^{**}P < 0.01$; $^{***}P < 0.001$).

Supplementary Material

Supplementary Material is available at *HMG* online.

Acknowledgements

Funding

References

1. Abrams, A.J., Hufnagel, R.B., Rebelo, A., Zanna, C., Patel, N., Gonzalez, M.A., Campeanu, I.J., Griffin, L.B., Groenewald, S., Strickland, A.V. et al. (2015) Mutations in SLC25A46, encoding a UGO1-like protein, cause an optic atrophy spectrum disorder. *Nat. Genet.*, **47**, 926–932.

2. Charlesworth, G., Balint, B., Mencacci, N.E., Carr, L., Wood, N.W. and Bhatia, K.P. (2016) SLC25A46 mutations underlie progressive myoclonic ataxia with optic atrophy and neuropathy. *Mov. Disord.*, **31**, 1249–1251.

3. Janer, A., Prudent, J., Paupe, V., Fahiminiya, S., Majewski, J., Sgarioto, N., Des Rosiers, C., Forest, A., Lin, Z.Y., Gingras, A.C. et al. (2016) SLC25A46 is required for mitochondrial lipid homeostasis and cristae maintenance and is responsible for Leigh syndrome. *EMBO Mol. Med.*, **8**, 1019–1038.

4. Nguyen, M., Boesten, I., Hellebrekers, D.M., Mulder-den Hartog, N.M., de Coo, I.F., Smeets, H.J. and Gerards, M. (2017) Novel pathogenic SLC25A46 splice-site mutation causes an optic atrophy spectrum disorder. *Clin. Genet.*, **91**, 121–125.

5. Wan, J., Steffen, J., Yourshaw, M., Mamsa, H., Andersen, E., Rudnik-Schoneborn, S., Pope, K., Howell, K.B., McLean, C.A., Kornberg, A.J. et al. (2016) Loss of function of SLC25A46 causes lethal congenital pontocerebellar hypoplasia. *Brain*, pii: aww212, DOI: 10.1093/brain/aww212

6. Steffen, J., Vashisht, A.A., Wan, J., Jen, J.C., Claypool, S.M., Wohlschlegel, J.A. and Koehler, C.M. (2017) Rapid degradation of mutant SLC25A46 by the ubiquitin-proteasome system results in MFN1/2-mediated hyperfusion of mitochondria. *Mol. Biol. Cell*, **28**, 600–612.

7. Sheng, Z.H. and Cai, Q. (2012) Mitochondrial transport in neurons: impact on synaptic homeostasis and neurodegeneration. *Nat. Rev. Neurosci.*, **13**, 77–93.

8. Olichon, A., Guillou, E., Delettre, C., Landes, T., Arnaune-Pelloquin, L., Emorine, L.J., Mils, V., Daloyau, M., Hamel, C., Amati-Bonneau, P. et al. (2006) Mitochondrial dynamics and disease, OPA1. *Biochim. Biophys. Acta*, **1763**, 500–509.

9. Knott, A.B., Perkins, G., Schwarzenbacher, R. and Bossy-Wetzel, E. (2008) Mitochondrial fragmentation in neurodegeneration. *Nat. Rev. Neurosci.*, **9**, 505–518.

10. Zorzano, A., Liesa, M. and Palacin, M. (2009) Mitochondrial dynamics as a bridge between mitochondrial dysfunction and insulin resistance. *Arch. Physiol. Biochem.*, **115**, 1–12.

11. Su, B., Wang, X., Zheng, L., Perry, G., Smith, M.A. and Zhu, X. (2010) Abnormal mitochondrial dynamics and neurodegenerative diseases. *Biochim. Biophys. Acta*, **1802**, 135–142.

12. Zuchner, S., Mersiyanova, I.V., Muglia, M., Bissar-Tadmouri, N., Rochelle, J., Dadali, E.L., Zappia, M., Nelis, E., Patitucci, A., Senderek, J. et al. (2004) Mutations in the mitochondrial GTPase mitofusin 2 cause Charcot-Marie-Tooth neuropathy type 2A. *Nat. Genet.*, **36**, 449–451.

13. Lawson, V.H., Graham, B.V. and Flanigan, K.M. (2005) Clinical and electrophysiologic features of CMT2A with mutations in the mitofusin 2 gene. *Neurology*, **65**, 197–204.

14. Cartoni, R. and Martinou, J.C. (2009) Role of mitofusin 2 mutations in the physiopathology of Charcot-Marie-Tooth disease type 2A. *Exp. Neurol.*, **218**, 268–273.

15. Alexander, C., Votruba, M., Pesch, U.E., Thiselton, D.L., Mayer, S., Moore, A., Rodriguez, M., Kellner, U., Leo-Kottler, B., Auburger, G. et al. (2000) OPA1, encoding a dynamin-related GTPase, is mutated in autosomal dominant optic atrophy linked to chromosome 3q28. *Nat. Genet.*, **26**, 211–215.

16. Delettre, C., Lenaers, G., Griffoin, J.M., Gigarel, N., Lorenzo, C., Belenguer, P., Pelloquin, L., Grosgeorge, J., Turc-Carel, C., Perret, E. *et al.* (2000) Nuclear gene OPA1, encoding a mitochondrial dynamin-related protein, is mutated in dominant optic atrophy. *Nat. Genet.*, **26**, 207–210.

17. Waterham, H.R., Koster, J., van Roermund, C.W., Mooyer, P.A., Wanders, R.J. and Leonard, J.V. (2007) A lethal defect of mitochondrial and peroxisomal fission. *N. Engl. J. Med.*, **356**, 1736–1741.

18. Olichon, A., Baricault, L., Gas, N., Guillou, E., Valette, A., Belenguer, P. and Lenaers, G. (2003) Loss of OPA1 perturbates the mitochondrial inner membrane structure and integrity, leading to cytochrome c release and apoptosis. *J. Biol. Chem.*, **278**, 7743–7746.

19. Lee, Y.J., Jeong, S.Y., Karbowski, M., Smith, C.L. and Youle, R.J. (2004) Roles of the mammalian mitochondrial fission and fusion mediators Fis1, Drp1, and Opa1 in apoptosis. *Mol. Biol. Cell*, **15**, 5001–5011.

20. Chen, H., Detmer, S.A., Ewald, A.J., Griffin, E.E., Fraser, S.E. and Chan, D.C. (2003) Mitofusins Mfn1 and Mfn2 coordinately regulate mitochondrial fusion and are essential for embryonic development. *J. Cell Biol.*, **160**, 189–200.

21. Chen, H., Chomyn, A. and Chan, D.C. (2005) Disruption of fusion results in mitochondrial heterogeneity and dysfunction. *J. Biol. Chem.*, **280**, 26185–26192.

22. Ishihara, N., Nomura, M., Jofuku, A., Kato, H., Suzuki, S.O., Masuda, K., Otera, H., Nakanishi, Y., Nonaka, I., Goto, Y. *et al.* (2009) Mitochondrial fission factor Drp1 is essential for embryonic development and synapse formation in mice. *Nat. Cell Biol.*, **11**, 958–966.

23. Wakabayashi, J., Zhang, Z., Wakabayashi, N., Tamura, Y., Fukaya, M., Kensler, T.W., Iijima, M. and Sesaki, H. (2009) The dynamin-related GTPase Drp1 is required for embryonic and brain development in mice. *J. Cell Biol.*, **186**, 805–816.

24. Girard, M., Lariviere, R., Parfitt, D.A., Deane, E.C., Gaudet, R., Nossova, N., Blondeau, F., Prenosil, G., Vermeulen, E.G., Duchen, M.R. *et al.* (2012) Mitochondrial dysfunction and Purkinje cell loss in autosomal recessive spastic ataxia of Charlevoix-Saguenay (ARSACS). *Proc. Natl. Acad. Sci. U. S. A*, **109**, 1661–1666.

25. Kageyama, Y., Zhang, Z., Roda, R., Fukaya, M., Wakabayashi, J., Wakabayashi, N., Kensler, T.W., Reddy, P.H., Iijima, M. and Sesaki, H. (2012) Mitochondrial division ensures the survival of postmitotic neurons by suppressing oxidative damage. *J. Cell Biol.*, **197**, 535–551.

26. Purnell, P.R. and Fox, H.S. (2013) Autophagy-mediated turnover of dynamin-related protein 1. *BMC Neurosci.*, **14**, 86.

27. Ikeda, Y., Shirakabe, A., Maejima, Y., Zhai, P., Sciarretta, S., Toli, J., Nomura, M., Mihara, K., Egashira, K., Ohishi, M. *et al.* (2015) Endogenous Drp1 mediates mitochondrial autophagy and protects the heart against energy stress. *Circ. Res.*, **116**, 264–278.

28. Jain, I.H., Zazzeron, L., Goli, R., Alexa, K., Schatzman-Bone, S., Dhillon, H., Goldberger, O., Peng, J., Shalem, O., Sanjana, N.E. *et al.* (2016) Hypoxia as a therapy for mitochondrial disease. *Science*, **352**, 54–61.

29. Zaqout, S. and Kaindl, A.M. (2016) Golgi-cox staining step by step. *Front. Neuroanat.*, **10**, 38.

30. Ehara, A. and Ueda, S. (2009) Application of Fluoro-Jade C in acute and chronic neurodegeneration models: utilities and staining differences. *Acta Histochem. Cytochem.*, **42**, 171–179.

31. Shih, E.K., Sekerkova, G., Ohtsuki, G., Aldinger, K.A., Chizhikov, V.V., Hansel, C., Mugnaini, E. and Millen, K.J. (2015) The Spontaneous Ataxic Mouse Mutant Tippy is

Characterized by a Novel Purkinje Cell Morphogenesis and Degeneration Phenotype. *Cerebellum*, **14**, 292–307.

32. Bereiter-Hahn, J. and Voth, M. (1994) Dynamics of mitochondria in living cells: shape changes, dislocations, fusion, and fission of mitochondria. *Microsc. Res. Tech.*, **27**, 198–219.

33. Baurle, J. and Grusser-Cornehls, U. (1994) Axonal torpedoes in cerebellar Purkinje cells of two normal mouse strains during aging. *Acta Neuropathol.*, **88**, 237–245.

34. Liu, X. and Hajnoczky, G. (2011) Altered fusion dynamics underlie unique morphological changes in mitochondria during hypoxia-reoxygenation stress. *Cell Death Differ.*, **18**, 1561–1572.

35. Ding, W.X., Li, M., Biazik, J.M., Morgan, D.G., Guo, F., Ni, H.M., Goheen, M., Eskelinen, E.L. and Yin, X.M. (2012) Electron microscopic analysis of a spherical mitochondrial structure. *J. Biol. Chem.*, **287**, 42373–42378.

36. Youle, R.J. and Narendra, D.P. (2011) Mechanisms of mitophagy. *Nat. Rev. Mol. Cell Biol.*, **12**, 9–14.

37. Hasegawa, T., Ueda, T., Okamoto, M. and Ogata, N. (2014) Presence of foveal bulge in optical coherence tomographic images in eyes with macular edema associated with branch retinal vein occlusion. *Am. J. Ophthalmol.*, **157**, 390–396. e391.

38. Semba, K., Namekata, K., Guo, X., Harada, C., Harada, T. and Mitamura, Y. (2014) Renin-angiotensin system regulates neurodegeneration in a mouse model of normal tension glaucoma. *Cell Death Dis.*, **5**, e1333.

39. Alavi, M.V., Bette, S., Schimpf, S., Schuettauf, F., Schraermeyer, U., Wehrl, H.F., Ruttiger, L., Beck, S.C., Tonagel, F., Pichler, B.J. *et al.* (2007) A splice site mutation in the murine Opa1 gene features pathology of autosomal dominant optic atrophy. *Brain*, **130**, 1029–1042.

40. Chen, H., McCaffery, J.M. and Chan, D.C. (2007) Mitochondrial fusion protects against neurodegeneration in the cerebellum. *Cell*, **130**, 548–562.

41. Davies, V.J., Hollins, A.J., Piechota, M.J., Yip, W., Davies, J.R., White, K.E., Nicols, P.P., Boulton, M.E. and Votruba, M. (2007) Opa1 deficiency in a mouse model of autosomal dominant optic atrophy impairs mitochondrial morphology, optic nerve structure and visual function. *Hum. Mol. Genet.*, **16**, 1307–1318.

42. Chang, C.R., Manlandro, C.M., Arnoult, D., Stadler, J., Posey, A.E., Hill, R.B. and Blackstone, C. (2010) A lethal de novo mutation in the middle domain of the dynamin-related GTPase Drp1 impairs higher order assembly and mitochondrial division. *J. Biol. Chem.*, **285**, 32494–32503.

43. Chang, D.T. and Reynolds, I.J. (2006) Mitochondrial trafficking and morphology in healthy and injured neurons. *Prog. Neurobiol.*, **80**, 241–268.

44. Mishra, P. and Chan, D.C. (2016) Metabolic regulation of mitochondrial dynamics. *J. Cell Biol.*, **212**, 379–387.

45. Cui, K., Luo, X., Xu, K. and Ven Murthy, M.R. (2004) Role of oxidative stress in neurodegeneration: recent developments in assay methods for oxidative stress and nutraceutical antioxidants. *Prog. Neuropsychopharmacol. Biol. Psychiatry*, **28**, 771–799.

46. Kern, J.K. and Jones, A.M. (2006) Evidence of toxicity, oxidative stress, and neuronal insult in autism. *J. Toxicol. Environ. Health. B Crit. Rev.*, **9**, 485–499.

47. Fatokun, A.A., Stone, T.W. and Smith, R.A. (2008) Oxidative stress in neurodegeneration and available means of protection. *Front. Biosci.*, **13**, 3288–3311.

48. Hayasaka, K., Himoro, M., Sato, W., Takada, G., Uyemura, K., Shimizu, N., Bird, T.D., Conneally, P.M. and Chance, P.F. (1993) Charcot-Marie-Tooth neuropathy type 1B is associated with mutations of the myelin P0 gene. *Nat. Genet.*, **5**, 31–34.

49. Robaglia-Schlupp, A., Pizant, J., Norreel, J.C., Passage, E., Saberan-Djoneidi, D., Ansaldi, J.L., Vinay, L., Figarella-Branger, D., Levy, N., Clarac, F. *et al.* (2002) PMP22 overexpression causes dysmyelination in mice. *Brain*, **125**, 2213–2221.

50. Chen, B., Gilbert, L.A., Cimini, B.A., Schnitzbauer, J., Zhang, W., Li, G.W., Park, J., Blackburn, E.H., Weissman, J.S., Qi, L.S. *et al.* (2013) Dynamic imaging of genomic loci in living human cells by an optimized CRISPR/Cas system. *Cell*, **155**, 1479–1491.

51. Valerius, M.T., Patterson, L.T., Witte, D.P. and Potter, S.S. (2002) Microarray analysis of novel cell lines representing two stages of metanephric mesenchyme differentiation. *Mech. Dev.*, **112**, 219–232.

52. Wang, H., Yang, H., Shivalila, C.S., Dawlaty, M.M., Cheng, A.W., Zhang, F. and Jaenisch, R. (2013) One-step generation of mice carrying mutations in multiple genes by CRISPR/Cas-mediated genome engineering. *Cell*, **153**, 910–918.

53. Esmailpour, T., Riazifar, H., Liu, L., Donkervoort, S., Huang, V.H., Madaan, S., Shoucri, B.M., Busch, A., Wu, J., Towbin, A. *et al.* (2014) A splice donor mutation in NAA10 results in the dysregulation of the retinoic acid signalling pathway and causes Lenz microphthalmia syndrome. *J. Med. Genet.*, **51**, 185–196.

54. Riazifar, H., Sun, G., Wang, X., Rupp, A., Vemaraju, S., Ross-Cisneros, F.N., Lang, R.A., Sadun, A.A., Hattar, S., Guan, M.X. *et al.* (2015) Phenotypic and functional characterization of Bst+/- mouse retina. *Dis. Model. Mech.*, **8**, 969–976.

55. Provencher, S.W. (1993) Estimation of metabolite concentrations from localized in vivo proton NMR spectra. *Magn. Reson. Med.*, **30**, 672–679.

56. Simon, M., Richard, E.M., Wang, X., Shahzad, M., Huang, V.H., Qaiser, T.A., Potluri, P., Mahl, S.E., Davila, A., Nazli, S. *et al.* (2015) Mutations of human NARS2, encoding the mitochondrial asparaginyl-tRNA synthetase, cause nonsyndromic deafness and Leigh syndrome. *PLoS Genet.*, **11**, e1005097.

57. Fukumitsu, K., Hatsukano, T., Yoshimura, A., Heuser, J., Fujishima, K. and Kengaku, M. (2016) Mitochondrial fission protein Drp1 regulates mitochondrial transport and dendritic arborization in cerebellar Purkinje cells. *Mol. Cell. Neurosci.*, **71**, 56–65.